Available online at www.sciencedirect.com

ScienceDirect

International Journal of Machine Tools & Manufacture 47 (2007) 1368–1380

INTERNATIONAL JOURNAL OF MACHINE TOOLS & MANUFACTURE DESIGN, RESEARCH AND APPLICATION

www.elsevier.com/locate/ijmactool

Shrink fit tool holder connection stiffness/damping modeling for frequency response prediction in milling

Tony L. Schmitz*, Kevin Powell, Dongki Won, G. Scott Duncan, W. Gregory Sawyer, John C. Ziegert

Department of Mechanical and Aerospace Engineering, University of Florida, Gainesville, FL 32611, USA

Received 21 June 2006; received in revised form 7 August 2006; accepted 10 August 2006
Available online 2 October 2006

Abstract

In this paper we present a finite element modeling approach to determine the stiffness and damping behavior between the tool and holder in thermal shrink fit connections. The continuous contact stiffness/damping profile between the holder and portion of the tool inside the holder is approximated by defining coordinates along the interface contact length and assigning position-dependent stiffness and equivalent viscous damping values between the tool and holder. These values are incorporated into the third generation receptance coupling substructure analysis (RCSA) method, which is used to predict the tool point frequency response for milling applications. Once the holder and inserted tool section are connected using the finite element analysis-based stiffness and damping values, this subassembly is then rigidly coupled to the (measured) spindle–holder base and (modeled) tool. Experimental validation is provided.

Keywords: Receptance; High-speed machining; Finite element

1. Introduction

Discrete part production by milling remains an important manufacturing capability. However, there are many potential obstacles to producing quality parts at low cost in a timely manner. One particular limitation that has received considerable attention in the literature is chatter, or unstable machining; a second is surface location error, or an error in the part dimension caused by dynamic deflections of the tool (and potentially the part/fixture) during stable cutting. In both cases, a primary factor affecting the process performance is the system frequency response function, or FRF.

The system FRF, often dominated by the flexibility of the tool–holder–spindle assembly as reflected at the tool's free end, can be obtained using impact testing, where an instrumented hammer is used to excite the tool at its free end (i.e., the tool point) and the resulting vibration is measured using an appropriate transducer, typically a low-mass accelerometer. However, due to the large number of spindle, holder, and tool combinations that may be available in a particular production facility, the required testing time can be significant. Further, the measured response is often strongly dependent on the tool overhang length. Therefore, a model which is able to predict the tool point response based on minimum input data is the preferred alternative [1–13].

The purpose of this paper is to build on the previous work of Schmitz et al. [1–8], which describes tool point FRF, or receptance, prediction using the receptance coupling substructure analysis (RCSA) method. In these previous studies, two- and three-component models of the machine–spindle–holder–tool assembly were defined. In the two-component model, the machine–spindle–holder displacement-to-force receptance was recorded at the free end of the holder using impact testing, while the tool was modeled analytically. The tool and machine–spindle–holder substructure receptances were then coupled through translational and rotational springs and dampers, where their values were determined through a nonlinear least squares fitting procedure. In this initial work the displacement-to-moment, rotation-to-force, and

---

*Corresponding author. Tel.: +352 392 8909; fax: +352 392 1071.
E-mail address: tschmitz@ufl.edu (T.L. Schmitz).

0890-6955/$ - see front matter © 2006 Elsevier Ltd. All rights reserved.
doi:10.1016/j.ijmachtools.2006.08.009

rotation-to-moment receptances at the free end of the holder were assumed zero (i.e., perfectly rigid).

In the second-generation three-component model, the machine–spindle–holder substructure was separated into two parts: (1) the machine, spindle, holder taper, and holder flange (or spindle–holder base subassembly); and (2) the remaining portion of the holder from the flange to the free end (the extended holder subassembly). The rotation-to-force/moment and displacement-to-moment receptances for the free end of the spindle–holder base subassembly were determined using displacement-to-force measurements and finite-difference computations. The experimental procedure involved recording direct and cross displacement-to-force measurements of a simple geometry 'standard' holder clamped in the spindle and calculating the receptances at the free end of the assembly by finite differences [5,6]. The portion of the standard holder beyond the flange was then removed in simulation using an inverse receptance coupling approach to identify the four spindle–holder base subassembly receptances (i.e., displacement/rotation-to-force/moment). These receptances were then coupled to models of the actual holder and tool. Again, to account for finite stiffness and energy dissipation (i.e., damping) in the tool–holder connection, the tool was coupled to the holder using translational and rotational springs and dampers, assembled in the matrix K (Eq. (1)), where k_{yf} is the displacement-to-force stiffness, $k_{\theta m}$ the rotation-to-moment stiffness, c_{yf} and $c_{\theta m}$ are the corresponding viscous damping terms, and ω is the circular frequency (rad/s). See Fig. 1. The portion of the holder with the tool inserted was treated using a composite modulus and mass in the event that the holder and tool materials were different, such as a steel holder and carbide tool.

$$K = \begin{bmatrix} k_{yf} + \mathrm{i}\omega c_{yf} & 0 \\ 0 & k_{\theta m} + \mathrm{i}\omega c_{\theta m} \end{bmatrix}. \tag{1}$$

In this work, we extend the three-component model to include multiple connections between the tool and holder along the interference contact within the holder (rather than at the end of the holder as before). This is shown schematically in Fig. 2, where multiple complex stiffness matrices, K_i, describe the connection parameters at each location. We believe this to be a preferred solution because the stiffness/damping is now located at the appropriate locations, rather than artificially at the junction between the portions of the tool inside and outside the holder. We note, however, that the coordinate-based stiffness/damping analysis is an approximation of the continuous contact stiffness/damping profile between the holder and portion of the tool inside the holder.

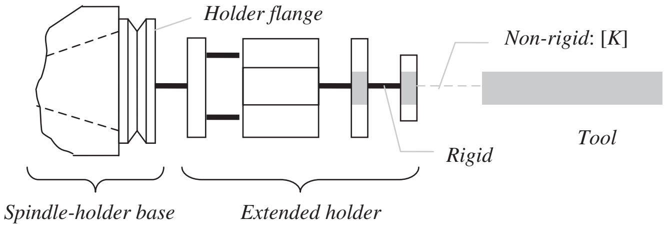

Fig. 1. Second generation RCSA model—the finite tool-holder stiffness/damping was represented by the empirical stiffness matrix, K, which was used to couple the overhung portion of the tool to the rest of the assembly. All other connections were rigid.

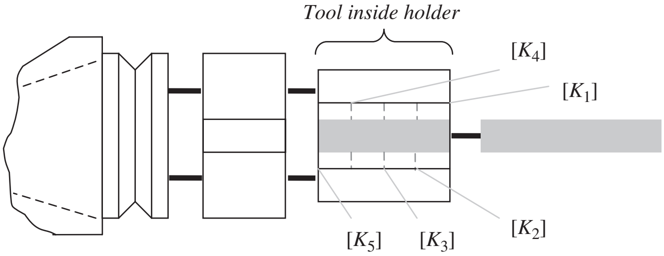

Fig. 2. Third generation RCSA model—the finite stiffness/damping between the tool and holder is represented by multiple K matrices determined from finite-element simulation.

In this new model the fully populated K matrix is defined as shown in Eq. (2), which now accounts for the displacement imposed by moment and the rotation caused by force through the nonzero off diagonal terms. Finite-element models are developed to determine the position-dependent stiffness and equivalent viscous damping values for a thermal shrink fit connection between the tool and holder, which represents the preferred interface for many high-speed milling applications. Using these values, the tool point FRF is predicted a priori and compared to measurements for a number of cases. No fitting parameters are applied in this analysis.

$$K = \begin{bmatrix} k_{yf} + \mathrm{i}\omega c_{yf} & k_{ym} + \mathrm{i}\omega c_{ym} \\ k_{\theta f} + \mathrm{i}\omega c_{yf} & k_{\theta m} + \mathrm{i}\omega c_{ym} \end{bmatrix}, \tag{2}$$

The paper is organized as follows. First, the RCSA approach for joining the portions of the tool and holder, which comprise the shrink fit connection is described. Second, the RCSA equation for the entire tool–holder–spindle assembly is provided. Third, finite-element modeling for the shrink fit connection is detailed. Fourth, experimental validation is provided. Finally, conclusions are presented.

2. Multiple point coupling for the tool–holder connection

To demonstrate the coupling between the concentric inner tool and outer holder components, the case of $n = 3$ connection coordinates, located at the ends of the contact length and at the mid-point, is now presented. The portions of the tool and holder in shrink fit contact are treated as free–free beams. For $n = 3$, a total of six component coordinates is obtained—three each on the internal tool and external holder (see Fig. 3) [14]. The component (i.e., tool and holder) displacement/rotations can be written as

$$\begin{aligned} &u_1 = R_{11}q_1 + R_{12}q_2 + R_{13}q_3, \quad u_2 = R_{21}q_1 + R_{22}q_2 + R_{23}q_3 \\ &u_3 = R_{31}q_1 + R_{32}q_2 + R_{33}q_3, \quad u_4 = R_{44}q_4 + R_{45}q_5 + R_{46}q_6, \\ &u_5 = R_{54}q_4 + R_{55}q_5 + R_{56}q_6, \quad u_6 = R_{64}q_4 + R_{65}q_5 + R_{66}q_6, \end{aligned} \tag{3}$$

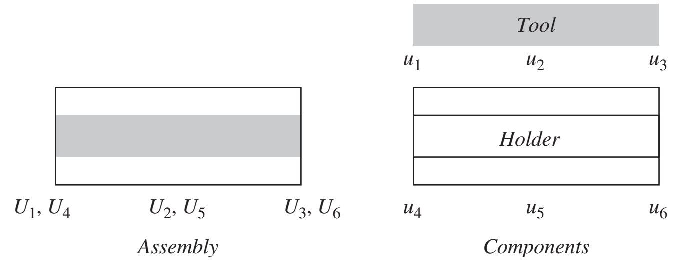

Fig. 3. Tool-in-holder assembly and components.

where a matrix formalism has been adopted [4,10]. Here, $u_i = \{y_i \quad \theta_i\}^{\mathrm{T}}$ are the component displacements/rotations; $q_i = \{f_i \quad m_i\}^{\mathrm{T}}$ are the component forces/moments; and

$$R_{ij}(\omega) = \begin{bmatrix} y_i/f_j & y_i/m_j \\ \theta_i/f_j & \theta_i/m_j \end{bmatrix} = \begin{bmatrix} h_{ij} & l_{ij} \\ n_{ij} & p_{ij} \end{bmatrix},$$

are the component receptances.

The compatibility conditions for the flexible/damped shrink fit connection are

$$K_1(u_4 - u_1) = -q_4, \quad K_2(u_5 - u_2) = -q_5,$$
$$\text{and} \quad K_3(u_6 - u_3) = -q_6, \tag{4}$$

where K_i is given by Eq. (2) and the component and assembly coordinates are defined at the same spatial locations so that $u_i = U_i$, $i = 1$–6. If the assembly direct response at the left end, $G_{11}(\omega)$, is to be determined, Q_1 is applied to coordinate U_1 of the assembly (the upper case variables denote assembly coordinates, forces, and moments). The equilibrium conditions are then:

$$q_1 + q_4 = Q_1, \quad q_2 + q_5 = 0, \quad \text{and} \quad q_3 + q_6 = 0. \tag{5}$$

The G_{11} matrix is determined in steps using the relevant equations. The first step is to insert the component displacement/rotation expressions into the compatibility conditions:

$$\begin{aligned} R_{11}q_1 + R_{12}q_2 + R_{13}q_3 &= R_{44}q_4 + R_{45}q_5 + R_{46}q_6 + K_1^{-1}q_4, \\ R_{21}q_1 + R_{22}q_2 + R_{23}q_3 &= R_{54}q_4 + R_{55}q_5 + R_{56}q_6 + K_2^{-1}q_5, \\ R_{31}q_1 + R_{32}q_2 + R_{33}q_3 &= R_{64}q_4 + R_{65}q_5 + R_{66}q_6 + K_3^{-1}q_6. \end{aligned} \tag{6}$$

The next step is to substitute $q_4 = Q_1 - q_1$, $q_5 = -q_2$, and $q_6 = -q_3$ and rearrange to obtain

$$\begin{bmatrix} R_{11} + R_{44} + K_1^{-1} & R_{12} + R_{45} & R_{13} + R_{46} \\ R_{21} + R_{54} & R_{22} + R_{55} + K_2^{-1} & R_{23} + R_{54} \\ R_{31} + R_{64} & R_{32} + R_{65} & R_{33} + R_{66} + K_3^{-1} \end{bmatrix} \begin{Bmatrix} q_1 \\ q_2 \\ q_3 \end{Bmatrix} = Q_1 \begin{bmatrix} R_{44} + K_1^{-1} \\ R_{54} \\ R_{64} \end{bmatrix}, \tag{7}$$

which gives the relationship between the component forces/moments and externally applied force/moment in matrix form. For this example, G_{11} can be expressed as

$$G_{11} = \frac{U_1}{Q_1} = \frac{u_1}{Q_1} = R_{11}\frac{q_1}{Q_1} + R_{12}\frac{q_2}{Q_1} + R_{13}\frac{q_3}{Q_1}, \tag{8}$$

so the ratios q_1/Q_1, q_2/Q_1, and q_3/Q_1 are required. These can be determined by rearranging Eq. (7):

$$\frac{1}{Q_1}\begin{Bmatrix} q_1 \\ q_2 \\ q_3 \end{Bmatrix} = \begin{bmatrix} R_{11} + R_{44} + K_1^{-1} & R_{12} + R_{45} & R_{13} + R_{46} \\ R_{21} + R_{54} & R_{22} + R_{55} + K_2^{-1} & R_{23} + R_{54} \\ R_{31} + R_{64} & R_{32} + R_{65} & R_{33} + R_{66} + K_3^{-1} \end{bmatrix}^{-1} \times \begin{bmatrix} R_{44} + K_1^{-1} \\ R_{54} \\ R_{64} \end{bmatrix} = [A],$$

where $[A]$ is a 6 by 2, or $2n$ by 2, by N matrix (N is the number of points in the frequency vector, ω). The reader may note that the matrix size is 6 by 2 because R_{ij} is a 2 by 2 matrix. The matrix A is partitioned as follows: the first two rows of A give q_1/Q_1; the second two rows provide q_2/Q_1; and the final two rows give q_3/Q_1. The desired direct receptances can then be computed from Eq. (8).

This 3-point coupling example can be extended to n coupling points by recognizing the recursive pattern in $[A]$. If the same coordinate numbering scheme is observed (i.e., coordinates 1 to n on the tool and $n+1$ to $2n$ on the holder), $[A]$ is given by

$$[A] = \begin{bmatrix} R_{11} + R_{n+1,n+1} + K_1^{-1} & R_{12} + R_{n+1,n+2} & \cdots & R_{1n} + R_{n+1,2n} \\ R_{21} + R_{n+2,n+1} & R_{22} + R_{n+2,n+2} + K_2^{-1} & \cdots & R_{2n} + R_{n+2,2n} \\ \vdots & \vdots & \ddots & \vdots \\ R_{n1} + R_{2n,n+1} & R_{n2} + R_{2n,n+2} & \cdots & R_{nn} + R_{2n,2n} + K_n^{-1} \end{bmatrix}^{-1} \times \begin{bmatrix} R_{n+1,n+1} + K_1^{-1} \\ R_{n+2,n+1} \\ \vdots \\ R_{2n,n+1} \end{bmatrix}.$$

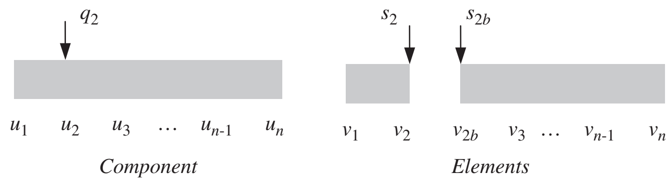

Fig. 4. Inner tool R_{12} determination.

This matrix can again be partitioned to find q_1/Q_1, $q_2/Q_1, \ldots, q_n/Q_1$. The assembly receptances G_{11} can then be found using $G_{11} = R_{11}(q_1/Q_1) + R_{12}(q_2/Q_1) + \cdots + R_{1n}(q_n/Q_1)$. The following sections detail the development of the required receptances, R_{ij}, for the inner tool and outer holder.

2.1. Inner tool receptances

The inner tool receptance matrix is composed of n^2 R_{ij} terms ($i = 1$–n and $j = 1$–n). However, by observing reciprocity (i.e., R_{ii} is symmetric and $R_{ji} = \begin{bmatrix} h_{ij} & n_{ij} \\ l_{ij} & p_{ij} \end{bmatrix}$), it is only necessary to determine the upper triangular portion of the square R_{ij} matrix, or $\sum_{i=1}^{n} i$ terms. The corners of the upper triangular portion of the matrix, R_{11}, R_{1n}, and R_{nn}, may be found using the closed-form receptances for uniform Euler–Bernoulli beams developed by Bishop and Johnson [15] directly, where the full beam length, L, is used in these computations[1]. The remaining terms in the first row of the R_{ij} matrix, $R_{12}, R_{13}, \ldots, R_{1,n-1}$ are determined next. To find R_{12}, q_2 is applied at coordinate u_2 as shown in Fig. 4.

The cylinder component must now be sectioned at coordinate u_2 into two elements with generalized receptance matrices E_{ij} and coordinates v_1 to v_n (see Fig. 4). For equally spaced connection coordinates, the length of the left element is $\Delta L = L/(n-1)$, while the right element length is L–ΔL. The element displacements/rotations can be written as

$$v_1 = E_{12}s_2, \quad v_2 = E_{22}s_2, \quad \text{and} \quad v_{2b} = E_{2b2b}s_{2b}, \tag{9}$$

where s_1, s_2, and s_{2b} are the nonzero element forces. The compatibility conditions for the rigid coupling between elements are given in Eq. (10). The associated equilibrium condition is provided in Eq. (11).

$$v_2 - v_{2b} = 0 \quad \text{and} \quad v_i = V_i, \quad i = 1 - n, \tag{10}$$

$$s_2 + s_{2b} = q_2. \tag{11}$$

Similar to the previous results, substitution of the element displacement/rotations and equilibrium condition into the compatibility conditions yields the following expression for R_{12}:

$$R_{12} = E_{12}(E_{22} + E_{2b2b})^{-1}E_{2b2b}. \tag{12}$$

To find R_{13}, q_3 is applied at u_3. The required left and right elements now have the lengths $2\Delta L$ and L–$2\Delta L$, respectively. The equation for R_{13} is

$$R_{13} = E_{13}(E_{33} + E_{3b3b})^{-1}E_{3b3b}. \tag{13}$$

The recursive pattern is immediately apparent so that R_{1j} is defined by

$$R_{1j} = E_{1j}(E_{jj} + E_{jbjb})^{-1}E_{jbjb}, \tag{14}$$

where $j = 2$ to n–1 is the column number.

Also, E_{1j} describes the cross-receptances for the left element (with a length of (j–1)ΔL), E_{ij} provides the direct receptances at the right end of the left element, and E_{jbjb} gives the direct receptances at the left end of the right element (with a length of L–(j–1)ΔL).

The nth column of the R_{ij} matrix is defined next. In this case, q_n is applied to the coordinate u_n at the right end of the cylinder component in order to find R_{in}, where $i = 2$ to n–1 is the row number. The recursive form is

$$R_{in} = E_{ii}(E_{ii} + E_{ibib})^{-1}E_{ibn}, \tag{15}$$

where E_{ii} and E_{ibib} are defined in the same way as E_{jj} and E_{jbjb}, respectively. The E_{ibn} cross-receptances for the right element are calculated using an element length of L–(i–1)ΔL.

The next terms to describe are the on-diagonal receptances R_{ii}, $i = 2$ to n–1. These can be written as

$$R_{ii} = E_{ii}(E_{ii} + E_{ibib})^{-1}E_{ibib}. \tag{16}$$

Again, E_{ii}, the direct receptances at the right end of the left element and E_{ibib}, the direct receptances at the left end of the right element, have the same definitions as previously provided.

The remaining receptances are those R_{ij} terms above the on-diagonal, exclusive of the 1st row and nth column. These receptances are determined column by column. For a particular column, $j = 2$ to n–1, R_{ij} is given by

$$R_{ij} = E_{ij}(E_{jj} + E_{jbjb})^{-1}E_{jbjb}, \quad i = 2 \text{ to } j - 1. \tag{17}$$

In this equation, the left element (with direct receptances E_{jj}) has a length of (j–1)ΔL and the right element (with direct receptances E_{jbjb}) has a length of L–(j–1)ΔL. However, the E_{ij} element receptances cannot be determined directly from the Bishop and Johnson formulation [15]. In this case, subelement receptances S_{ij} must be defined. This is demonstrated by solving for R_{23}.

To find R_{23}, q_3 is applied to coordinate u_2. The cylinder component is then split at coordinate u_3 to define two elements (see Fig. 5). The element displacements/rotations are given by

$$v_2 = E_{23}s_3, \quad v_3 = E_{33}s_3, \quad \text{and} \quad v_{3b} = E_{3b3b}s_{3b}. \tag{18}$$

The rigid connection compatibility conditions are shown in Eq. (19) and the equilibrium condition in Eq. (20).

$$v_3 - v_{3b} = 0, \quad \text{and} \quad v_i = u_i, \quad i = 1 - n, \tag{19}$$

$$s_3 + s_{3b} = q_3. \tag{20}$$

---

[1] Alternately, Timoshenko beam receptances can be applied.

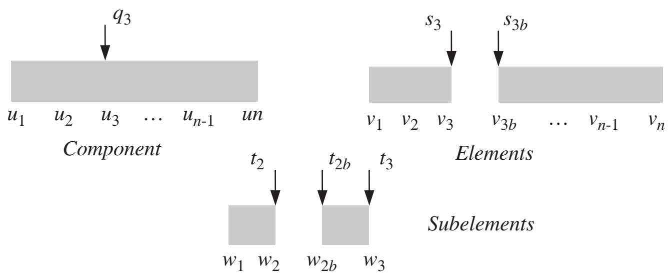

Fig. 5. Inner tool R_{23} determination.

Using these equations, it is found that

$$R_{23} = E_{23}(E_{33} + E_{3b3b})^{-1}E_{3bi3}. \tag{21}$$

As noted, E_{23}, the cross-receptances at coordinate v_2 of the left element due to the application of s_3 at coordinate v_3, is determined by separating the left element (with a length of $(j-1)\Delta L$), into two subelements at coordinate v_2 (see Fig. 5). The length of the left subelement is $(i-1)\Delta L = (2-1)\Delta L = \Delta L$, while the length of the right subelement is $(j-i)\Delta L = (3-2)\Delta L = \Delta L$.

Using the displacement/rotation, compatibility, and equilibrium equations, it is found that

$$E_{23} = S_{22}(S_{22} + S_{2b2b})^{-1}S_{2b3}, \tag{22}$$

where S_{22} gives the direct receptances at the right end of the left subelement, S_{2b2b} contains the direct receptances at the left end of the right subelement, and S_{2b3} represents the cross-receptances for the right subelement. The recursive formulation for this equation is

$$E_{ij} = S_{ii}(S_{ii} + S_{ibib})^{-1}S_{ibj}, \quad i = 2 \text{ to } j-1, \quad \text{and} \quad j = 2 \text{ to } n-1. \tag{23}$$

All terms in the upper triangular portion of the R_{ij} matrix for the inner cylinder have now been determined. The lower triangular portion, excluding the on-diagonal terms, is found by observing the symmetry rules given previously as demonstrated by the following pseudo-code.

```
for $i = 1$ to $n-1$,
    for $j = i+1$ to $n$,
        $R_{ji} = \begin{bmatrix} h_{ij} & n_{ij} \\ l_{ij} & p_{ij} \end{bmatrix}$,
    next $j$,
next $i$.
```

2.2. Outer holder receptances

To find the R_{ij} matrix for the outer holder, n is added to each coordinate number (i.e., the coordinate number for the tube left end is $n+1$ and the right end coordinate number is $2n$) and the beam geometry and material properties are updated for the receptance computations. All other definitions remain the same.

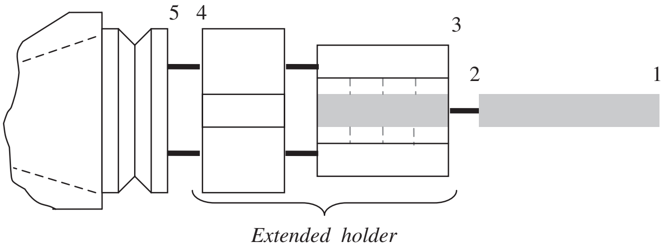

Fig. 6. Third generation RCSA model—coordinate definitions.

3. Tool–holder–spindle assembly RCSA equation

Once the shrink fit connection stiffness is incorporated into the tool–holder assembly (for the portion of the tool inside the holder) as defined in Section 2, the remaining components can be rigidly coupled. Assembly coordinate definitions for the overhung portion of the tool (1–2), extended holder (3–4), and spindle–holder base (5) are shown in Fig. 6. The corresponding RCSA equation for the assembly receptances at the tool point is obtained by: (1) rigidly coupling the overhung free–free tool to the free–free tool-extended holder to determine the new subassembly direct receptances at each end, GS_{11} and GS_{44}, and the cross-receptances, GS_{14} and GS_{41}; and (2) using the standard holder and finite-difference calculations to determine the four receptances at the free end of the standard holder (mounted in the spindle in question), removing the portion of the standard holder beyond the flange using inverse RCSA, and defining the direct receptance at the free end of the spindle–holder base subassembly, GS_{55}. See Eq. (24), where $H_{11}(\omega) = Y_1/F_1$ is the frequency response generally required for milling stability and surface location error analyses. Additional details are available in [5,6].

$$G_{11} = \begin{bmatrix} H_{11} & L_{11} \\ N_{11} & P_{11} \end{bmatrix} = GS_{11} - GS_{14}(GS_{44} + GS_{55})^{-1}GS_{41}. \tag{24}$$

4. Shrink fit connection finite-element modeling

Finite-element models for selected tool–holder assemblies were constructed using ANSYS. The boundary conditions were set as fixed-free and only the extended holder and tool were modeled (the flange and holder taper were considered part of the spindle–holder base, which was not included in this portion of the analysis). An example model for a 19.1 mm diameter carbide tool blank inserted in a steel tapered shrink fit holder is shown in Fig. 7 (FRF predictions for this model are provided in Section 5.1). In this example, 6324 20-node cubic elements (SOLID184), 768 8-node contact elements (CONTA174), and 768 8-node

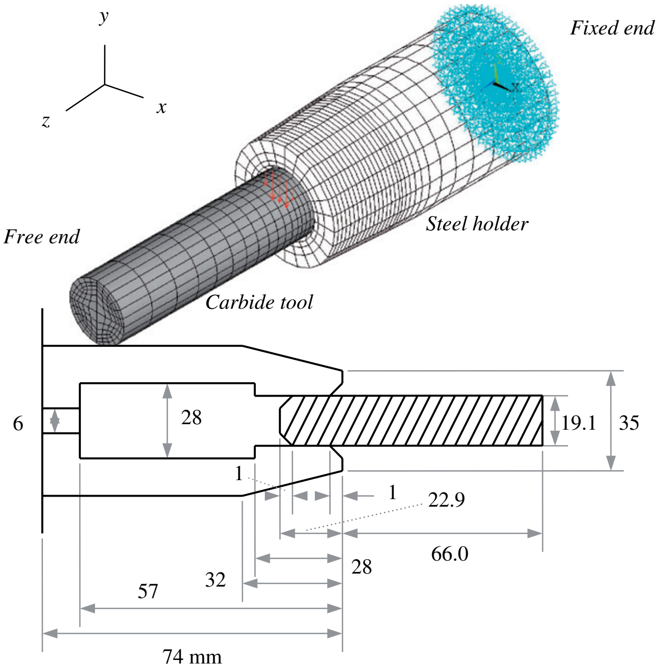

Fig. 7. Finite-element model for 19.1 mm diameter carbide tool blank inserted in steel tapered shrink fit holder. The base of the holder was held fixed, while the end of the tool was unsupported.

Table 1
Tool and holder material properties for finite-element simulations

	E (GPa)	ρ (kg/m^3)	υ	μ
Tool	560	14 400	0.22	0.15
Holder	200	7850	0.29	

target elements (TARGE170) were applied, where the flexible-to-flexible contact/target elements were located at the interface between the tool and holder; this gave a total of 29 467 nodes. The coordinate directions for the model were: x—horizontal, y—vertical, z—along the tool axis. The material properties are defined in Table 1, where E is the elastic modulus, ρ the mass density, υ the Poisson's ratio, and μ the friction coefficient. The reader may note that these are mean values from the literature. Carbide properties, in particular, may vary somewhat from these assumed values.

The finite-element simulations were carried out in two primary time intervals of 1 s each. In the first interval, the contact pressure between the tool and holder was allowed to grow due to the imposed radial interference. Fig. 8 shows the contact pressure, P, profile for the model in Fig. 7 with a 10 μm radial interference. In the second interval, the y direction force or couple was applied to the tool just beyond the end of contact. The forces were applied using an equivalent nodal force arrangement (to minimize localized deformation effects), where 25% of the total force is applied at each of three central nodes and 12.5% is applied at each of two outer nodes. For both intervals, time was divided into five steps as shown in Fig. 9 (force application is demonstrated).

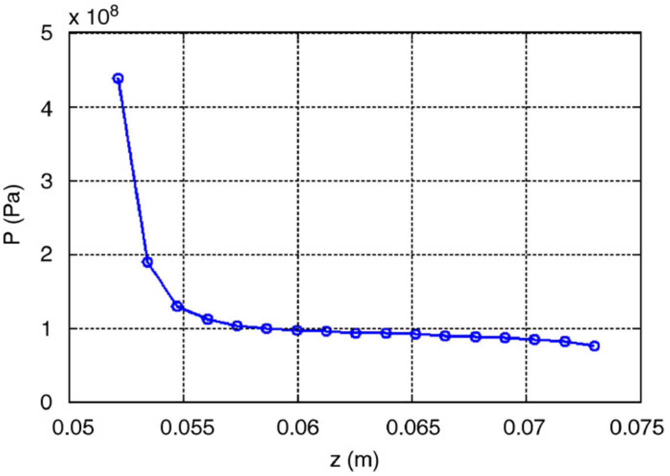

Fig. 8. Simulated contact pressure profile for the shrink fit tool–holder interface (10 μm radial interference) modeled in Fig. 7. The z-axis origin is located at the fixed end of the holder.

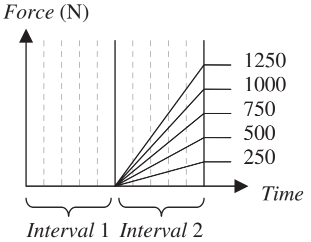

Fig. 9. Time intervals for finite-element simulation: (1) interference pressure; (2) y force application.

4.1. Stiffness

Using the model described in the previous paragraphs, the position-dependent stiffness values were determined using the following steps. At the end of the two time intervals (pressure growth followed by force or moment application), the y direction displacements of the tool at nodes along the tool top centerline were recorded. The y displacements, as a function of z location, imposed by the force/couple were then computed by differencing the two results. By applying a range of forces (250–1250 N in steps of 250 N) and couples (2.5–12.5 N m in steps of 2.5 N m), the $k_{yf}(z)$ and $k_{ym}(z)$ stiffness values from Eq. (2) were calculated directly from the slope of the load–displacement curves for each node under consideration. For the $k_{\theta f}(z)$ and $k_{\theta m}(z)$ stiffness values, the rotation was first calculated by central finite difference from the displacement data, then the stiffness values were obtained from the load–rotation curve slope values. Example results for the tool–holder combination in Fig. 7 (10 μm radial interference) are provided in Fig. 10. It is seen that the finite differences

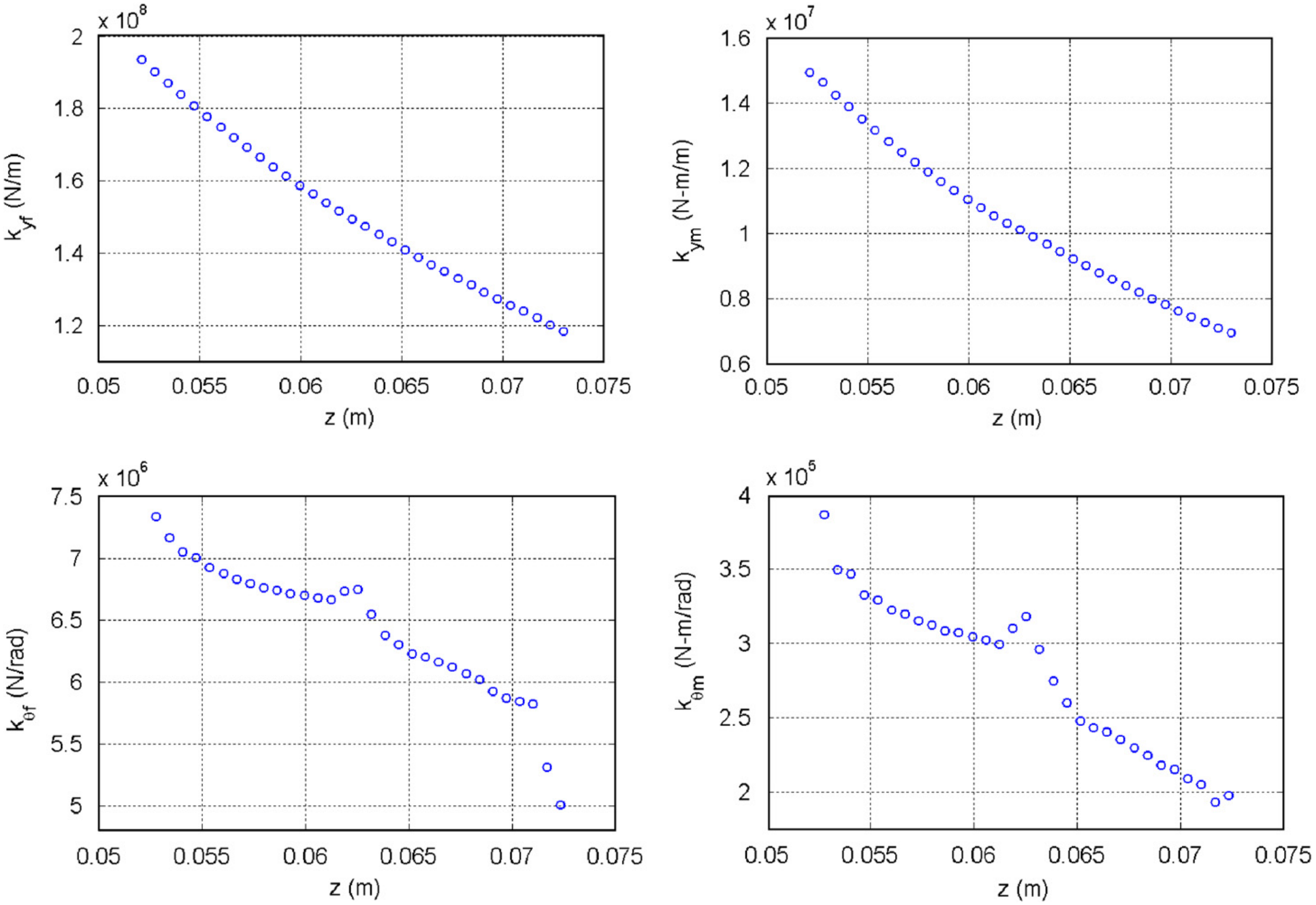

Fig. 10. Stiffness values for the finite-element model shown in Fig. 7 (10 μm radial interference).

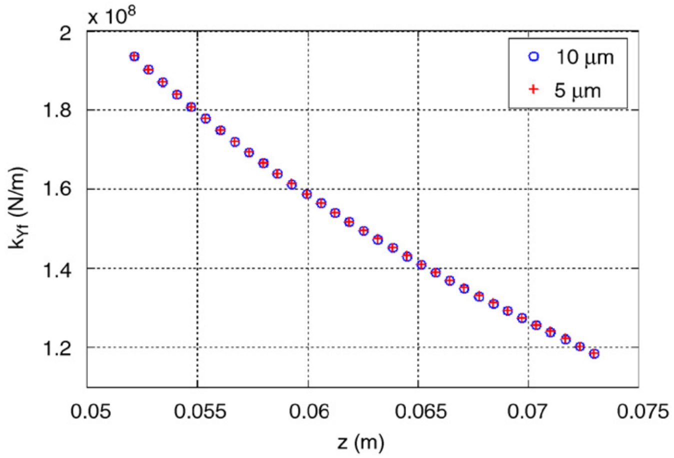

Fig. 11. Displacement-to-force stiffness variation with radial interference. Low sensitivity is observed.

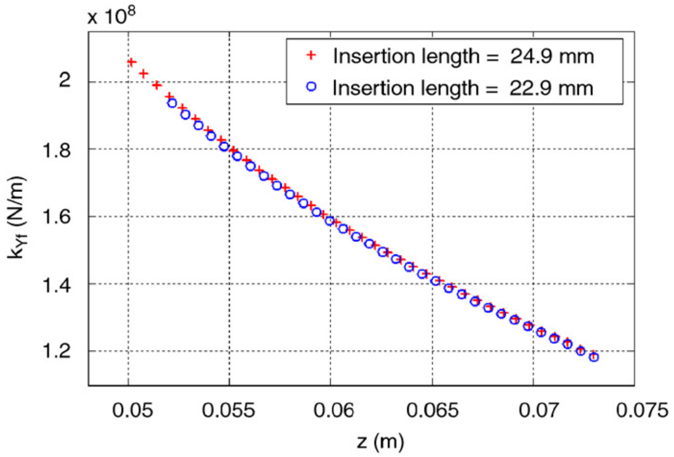

Fig. 12. Displacement-to-force stiffness variation with insertion length. As expected, the stiffness increases with insertion length, but the sensitivity is not high.

used to compute the rotations introduced some numerical noise.

Aside from the material properties, the primary variables in the shrink fit connection are the radial interference and tool insertion length. The sensitivity of the stiffness values shown in Fig. 10 to these variables was evaluated. Fig. 11 shows the $k_{yf}(z)$ results for radial interference values of 5 and 10 μm. Very little sensitivity is seen. Fig. 12 shows the

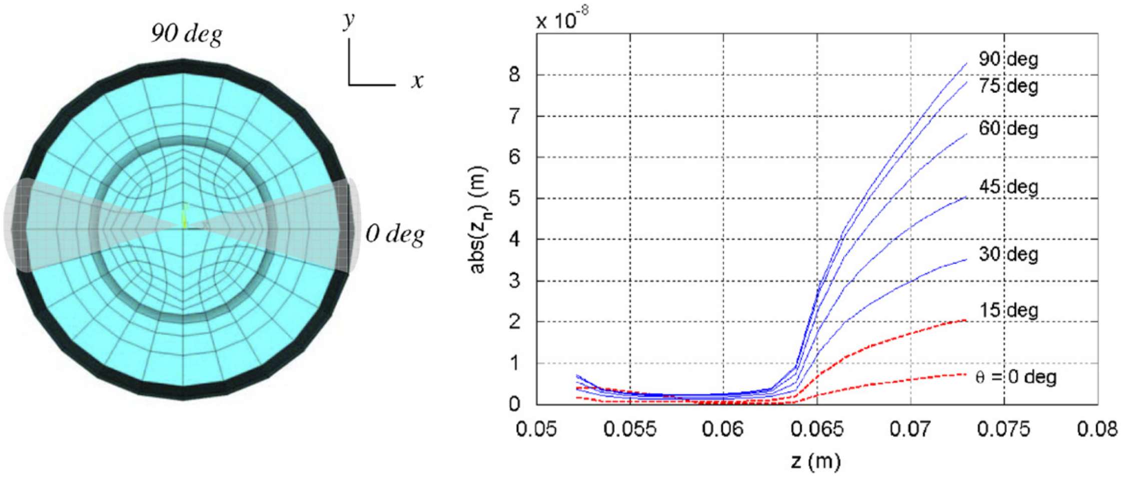

Fig. 13. (Left) End view of tool mesh—the shaded regions within 15° of the neutral axis were excluded from the damping calculations due to the geometric constraint on z-axis slip. (Right) Slip values for various angular values around the tool circumference (the 0° and 15° results were not used).

$k_{yf}(z)$ values for two different insertion lengths (22.9 and 24.9 mm). As expected, higher insertion length gives higher stiffness, but the sensitivity is not high.

4.2. Damping

We assumed that energy dissipation in the shrink fit connection occurred due to relative micro-slip between the tool and holder along the tool axis during the force/couple application. This Coulomb damping was converted to position-dependent equivalent viscous damping values by: (1) computing the friction (damping) force, F_d, for each element, n; (2) calculating the viscous damping value for each element according to Eq. (25) [16], where $|z_n|$ is the absolute value of the contact element displacement along the tool axis[2]; and (3) summing the damping values for the elements located around the tool circumference for the selected z location. It should be noted that the slip for elements close to the bending neutral axis was nearly zero. This would imply very high damping using the equivalent viscous damping approach; however, since it was due to a geometric constraint, the very small slip does not necessarily indicate increased damping and elements located $\pm 15°$ from the neutral axis were excluded from the analysis. Fig. 13 displays the end view of the tool mesh and the portions of the circumference used for the damping calculations. It also shows the corresponding slip values, $|z_n|$, due to a 250 N y direction force for angles, θ, from the neutral axis (0°) to the tool top centerline (90°) as a function of the z location.

$$c_{\mathrm{eq},n} = \frac{4 \times F_{d,n}}{\pi\omega|z_n|}. \tag{25}$$

The friction force was calculated from the product of the element area, element contact pressure (see Fig. 8, for example), and the assumed coefficient of friction (see Table 1). Because the work done by the friction force is path dependent, the $c_{\mathrm{eq},n}$ calculations were completed at each of the five steps in the second time interval and the results summed. This process was repeated two times. First, a range of forces (250–1250 N in steps of 250 N) was applied to determine the $c_{yf}(z)$ values. Second, couples (2.5–12.5 N m in steps of 2.5 N m) were applied to find the $c_{ym}(z)$ values. The analysis was the same in both cases. The respective damping values for the rotation terms in the K matrices (i.e., the bottom row in Eq. (2)) were taken to be equal to the previous results. The top panel in Fig. 14 shows the results for y direction forces of 250 and 1250 N, while the bottom panel displays the results for 2.5 and 12.5 N m applied moments. It is seen that the lower force/moment values cause less slip and, therefore, lead to higher equivalent viscous damping values.

5. Experimental results

5.1. Shrink fit holder with varying tool length

In this study 30 carbide tool blanks were sequentially inserted in the tapered thermal shrink fit holder modeled in Fig. 7 and the tool point response was recorded. The insertion length was maintained at 22.9 mm while the overhang length varied from 66.0 to 142.2 mm in increments of 2.5 mm (the 139.7 overhang length test was not completed) for the 19.1 mm diameter tool blanks. These measurements were completed on a 16 000 rpm direct drive spindle with an HSK 63A spindle–holder interface.

The substructure model is depicted in Fig. 15; the relevant dimensions are given in Table 2, where d_o is the outer diameter, d_i the inner diameter, and L the length. The material properties for the tool blanks and holder were provided in Table 1. In this case, the inner tool and outer holder within the shrink fit contact region (substructure II) were coupled using an appropriate K matrix at each end of

---

[2] The absolute value was required because the slip changed sign between the upper and lower surfaces of the tool.

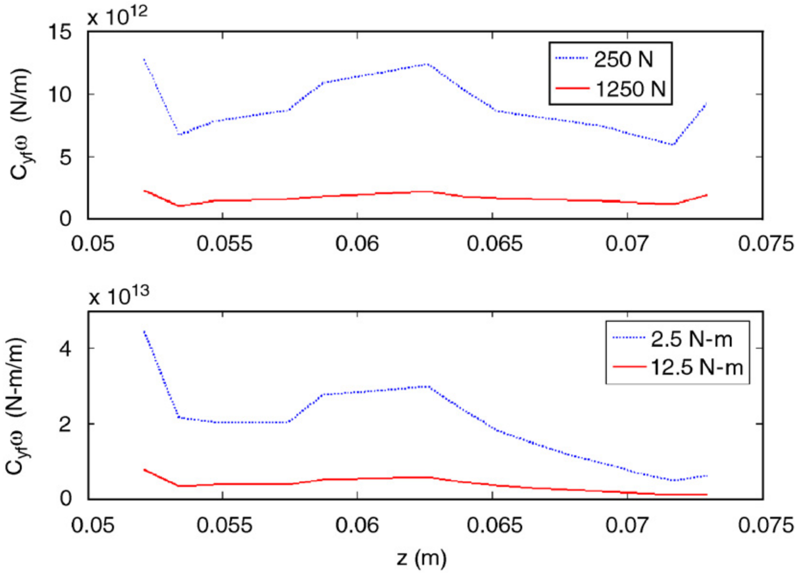

Fig. 14. (Top) Equivalent viscous damping values for y direction forces applied to the tool at the end of the contact length. (Bottom) Damping values for applied moments.

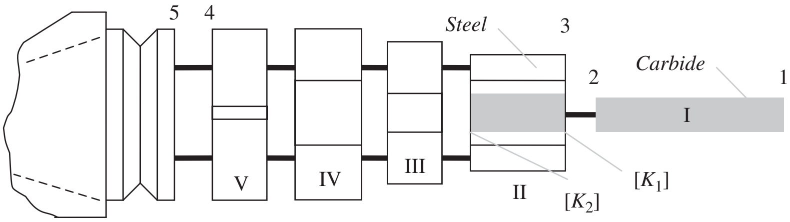

Fig. 15. Substructures for tool length overhang study. The inner tool and outer holder in substructure II were coupled using two K matrices (one at each end).

Table 2
Substructure dimensions for study of tool overhang length variation

Value (mm)	Substructure				
	V	VI	III	II	I
d_o	38.5	38.2	37.3	36.1	19.1
d_i	6.0	21.0	19.1	19.1	—
L	17.0	25.0	9.1	22.9	Varied

Table 3
K matrix values ($N = 2$) for study of tool overhang length variation

	Left	Right
k_{yf} (N/m)	1.89×10^8	1.15×10^8
k_{ym} (N m/m)	1.43×10^7	0.65×10^7
$k_{\theta f}$ (N/rad)	7.28×10^6	5.48×10^6
$k_{\theta m}$ (N m/rad)	3.63×10^5	1.84×10^5
$c_{yf}\omega$ (N/m)	5.23×10^{12}	
$c_{ym}\omega$ (N m/m)	1.10×10^{13}	

the contact ($N = 2$)[3]. The four stiffness values required to populate the two K matrices were determined from linear regressions to the finite-element results shown in Fig. 10. The two damping values were taken to be the average of all z locations for the minimum and maximum applied force/moment values from Fig. 14 since a clear linear trend was not evident. The entries for the left (i.e., at the fully inserted end of the contact in Fig. 15) and right (i.e., at the free end of the contact) K matrices are provided in Table 3. The receptances for the substructures I, III, IV, and V were determined using the Timoshenko beam formulation (100 elements were used in all instances) [17–19]. The substructure II receptances were computed as described in Section 2 using Bishop and Johnson's closed-form solutions for Euler–Bernoulli beams [15]. In both cases, the frequency-independent damping coefficient for the holder and tool was taken to be 0.0015.

A comparison of the 30 measurements and predictions is shown in Fig. 16. The top panel shows the measurements (log–linear magnitude with a range of 4×10^{-7}–4×10^{-5}

---

[3] Through simulation, it was determined that the addition of more connection coordinates ($N>2$) did not appreciably change the predicted assembly frequency responses.

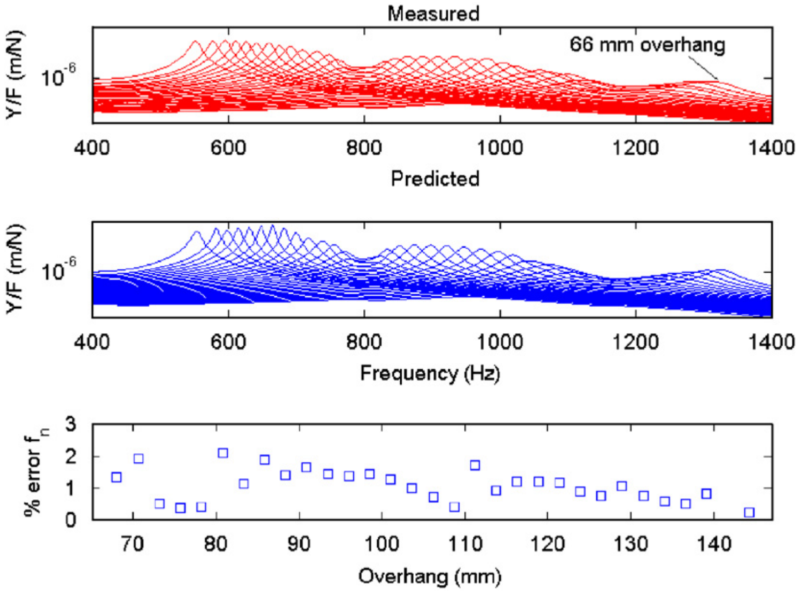

Fig. 16. Top—measured FRF magnitudes (log–linear scale) for 30 tool overhang lengths (66.0 mm FRF is identified); middle—predicted magnitudes using $N = 2\,K$ matrices; and bottom—percent difference between measured and predicted (dominant) natural frequencies, f_n.

m/N vs. frequency in Hz); the middle panel displays the predictions (same scale); and the bottom panel shows the percent difference between the measured and predicted (dominant) natural frequencies as a function of the tool overhang length. Agreement of 2% or better is observed for all 30 cases. It is also seen in the top two panels that, although the general trend is increased amplitude and reduced frequency with increasing overhang length, the tool point magnitudes are attenuated near 800 and 1200 Hz. This is due to dynamic interaction between the tool/holder clamped-free fundamental mode and the spindle modes at these frequencies [20].

Table 4
K matrix values ($N = 2$) for varying tool geometry study

Case		Left	Right
1	k_{yf} (N/m)	1.05×10^8	6.31×10^7
	k_{ym} (N m/m)	1.89×10^9	9.80×10^8
	$k_{\theta f}$ (N/rad)	4.74×10^6	3.87×10^6
	$k_{\theta m}$ (N m/rad)	6.40×10^7	4.26×10^7
	$c_{yf}\omega$ (N/m)	1.03×10^{13}	
	$c_{ym}\omega$ (N m/m)	5.50×10^{14}	
2	k_{yf} (N/m)	1.05×10^8	6.31×10^7
	k_{ym} (N m/m)	1.89×10^9	9.80×10^8
	$k_{\theta f}$ (N/rad)	4.74×10^6	3.87×10^6
	$k_{\theta m}$ (N m/rad)	6.43×10^7	4.24×10^7
	$c_{yf}\omega$ (N/m)	1.03×10^{13}	
	$c_{ym}\omega$ (N m/m)	3.18×10^{14}	
3	k_{yf} (N/m)	3.33×10^8	2.15×10^8
	k_{ym} (N m/m)	3.44×10^{10}	1.77×10^{10}
	$k_{\theta f}$ (N/rad)	1.82×10^7	1.25×10^7
	$k_{\theta m}$ (N m/rad)	1.16×10^6	7.41×10^5
	$c_{yf}\omega$ (N/m)	8.77×10^{12}	
	$c_{ym}\omega$ (N m/m)	4.42×10^{13}	

5.2. *Shrink fit holders with varying tool geometries*

In a second study 19.1 and 25.4 mm diameter carbide tool blanks were inserted in shrink fit holders using different insertion and overhang lengths. The spindle–holder interface for the 25 000 rpm spindle was HSK 63A. Results are presented for the following cases: (1) 19.1 mm diameter tool (101.6 overall), 25.4 mm insertion length; (2) 19.1 mm diameter (152.4 overall), 25.4 mm insertion; and (3) 25.4 mm diameter (152.4 mm overall), 25.4 mm insertion. The constant cross-section substructures were again modeled as shown in Fig. 15. The material properties in Table 1 were applied and the K matrix values ($N = 2$) are provided in Table 4.

Experimental results are provided in Figs. 17–19. The real and imaginary parts (linear scale) of the measured (dotted line) and predicted (solid line) results are shown. In Fig. 17, good agreement is observed for Case 1. A notable exception is the increased amplitude for the predicted spindle mode near 400 Hz. The cause for this disagreement is presumably due to inaccuracy in the standard holder measurements which propagate to the spindle–holder base subassembly receptances and, subsequently, to the tool point response predictions. For the Case 2 result in Fig. 18, the tool overhang length increase results in a decrease in the fundamental bending frequency to a value near the 400 Hz spindle mode. As demonstrated in Fig. 16, interaction occurs between the spindle and tool modes. Because the predicted spindle mode is too flexible, this interaction is stronger in the predicted case and yields separated modes for the assembly response. The interaction is also apparent in the measured case, but there is less separation due to the stiffer spindle mode. This effect is

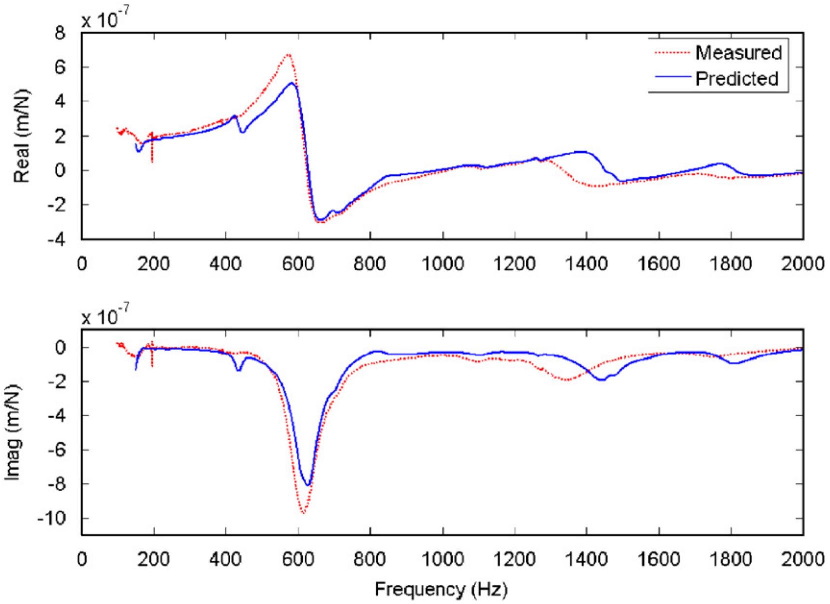

Fig. 17. Case 1 results—19.1 mm diameter tool (101.6 overall), 25.4 mm insertion length. The spindle mode near 400 Hz is too flexible in the predicted response (solid line).

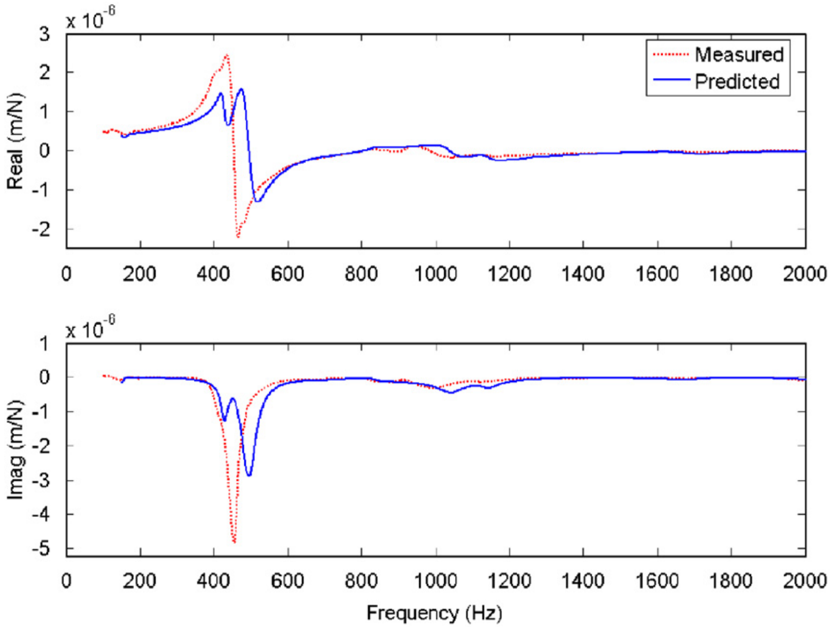

Fig. 18. Case 2 results—19.1 mm diameter tool (152.4 overall), 25.4 mm insertion length. Interaction between the tool and spindle mode near 400 Hz is stronger in the predicted response (solid line).

again observed in Case 3 (Fig. 19). The 25.4 mm diameter tool (same overhang as Case 2) again gives a fundamental bending frequency near the 400 Hz spindle mode. The exaggerated interaction is seen, although the tool mode is now slightly to the left of the spindle mode.

6. Conclusion

This paper describes the third generation receptance coupling substructure analysis (RCSA) model for tool point frequency response prediction. We extended the three-component model to include multiple connections between the tool and holder along the interference contact within the holder. We believe this to be a preferred solution because the stiffness/damping is now located at the appropriate locations, rather than artificially at the junction between the portions of the tool inside and outside the holder. Finite-element models were developed to determine the position-dependent stiffness and equivalent viscous damping values for a thermal shrink fit

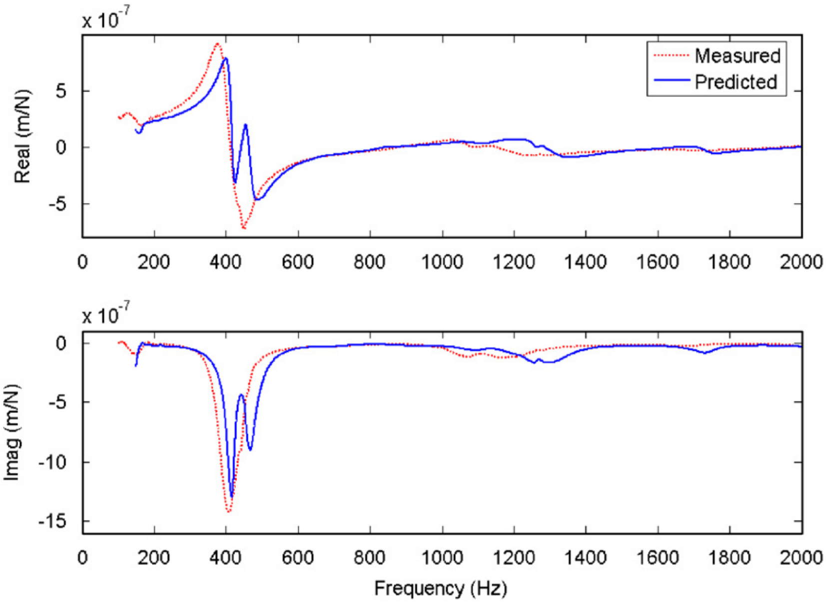

Fig. 19. Case 3 results—25.4 mm diameter tool (152.4 overall), 25.4 mm insertion length. Interaction between the tool and spindle mode near 400 Hz is again stronger in the predicted response (solid line).

connection between the tool and holder. Predictions of the tool point frequency response were completed and measurements of the modeled spindle–holder–tool assemblies were performed. The results generally agreed, although sensitivity of the assembly response to accurate identification of spindle–holder base receptances was demonstrated in specific instances.

Acknowledgments

This work was supported by the National Science Foundation (DMI-0238019), the Office of Naval Research (Young Investigator Program), and TechSolve. The authors wish to acknowledge contributions to the development of the RCSA method by Dr. M. Davies, University of North Carolina-Charlotte and Dr. T. Burns, National Institute of Standards and Technology. They also acknowledge Mr. Duke Hughes and Dr. P. Jacobs, BWXT Y-12, for their assistance in collecting portions of the data for this study. Finally, the three-component RCSA approach is patent pending.

References

[1] T. Schmitz, R. Donaldson, Predicting high-speed machining dynamics by substructure analysis, Annals of the CIRP 49 (1) (2000) 303–308.

[2] T. Schmitz, M. Davies, M. Kennedy, Tool point frequency response prediction for high-speed machining by RCSA, Journal of Manufacturing Science and Engineering 123 (2001) 700–707.

[3] T. Schmitz, M. Davies, K. Medicus, J. Snyder, Improving high-speed machining material removal rates by rapid dynamic analysis, Annals of the CIRP 50 (1) (2001) 263–268.

[4] T. Schmitz, T. Burns, Receptance coupling for high-speed machining dynamics prediction, in: Proceedings of the 21st International Modal Analysis Conference, 3–6 February 2003 (on CD).

[5] T. Schmitz, G.S. Duncan, Three-component receptance coupling substructure analysis for tool point dynamics prediction, Journal of Manufacturing Science and Engineering 127 (4) (2005) 781–790.

[6] T. Schmitz, G.S. Duncan, C. Zahner, J. Dyer, M. Tummond, Improved milling capabilities through dynamics prediction: three component spindle–holder–tool model, in: Proceedings of the 2005 National Science Foundation DMII Grantees Conference, 3–6 January 2005 (on CD).

[7] T. Burns, T. Schmitz, A study of linear joint and tool models in spindle–holder–tool receptance coupling, in: Proceedings of the 2005 American Society of Mechanical Engineers International Design Engineering Technical Conferences and Computers and Information in Engineering Conference, DETC2005-85275, 24–28 September 2005.

[8] C.-H. Cheng, T. Schmitz, N. Arakere, G.S. Duncan, An approach for micro-end-mill frequency response predictions, in: Proceedings of the American Society of Mechanical Engineers International Mechanical Engineering Congress and Exposition, IMECE2005-81215, 5–11 November 2005.

[9] A.S. Yigit, A.G. Ulsoy, Dynamic stiffness evaluation for reconfigurable machine tools including weakly non-linear joint characteristics, Proceedings of the I MECH E Part B—Journal of Engineering Manufacture 216 (1) (2002) 87–101.

[10] S. Park, Y. Altintas, M. Movahhedy, Receptance coupling for end mills, International Journal of Machine Tools and Manufacture 44 (11) (2003) 1151–1161.

[11] E.B. Kivanc, E. Budak, Structural modeling of end mills for form error and stability analysis, International Journal of Machine Tools and Manufacture 44 (11) (2004) 1151–1161.

[12] J. Agapiou, A methodology to measure joint stiffness parameters for toolholder/spindle interfaces, Transactions of NAMRI/SME 32 (2004) 503–510.

[13] G.P. Zhang, Y.M. Huang, W.H. Shi, W.P. Fu, Predicting dynamic behaviors of a whole machine tool structure based on computer-aided engineering, International Journal of Machine Tools and Manufacture 43 (2003) 699–706.

[14] T. Schmitz, G.S. Duncan, Receptance coupling for dynamics prediction of assemblies with coincident neutral axes, Journal of Sound and Vibration 289 (4–5) (2006) 1045–1065.

[15] R.E.D. Bishop, D.C. Johnson, The Mechanics of Vibration, Cambridge University Press, Cambridge, 1960.

[16] W. Thomson, M. Dahleh, Theory of Vibration with Applications, fifth ed., Prentice-Hall, Upper Saddle River, NJ, 1998.

[17] W. Weaver Jr., P. Timoshenko, D. Young, Vibration Problems in Engineering, fifth ed., Wiley, New York, 1990.

[18] T. Yokoyama, Vibrations of a hanging Timoshenko beam under gravity, Journal of Sound and Vibration 141 (2) (1990) 245–258.

[19] J. Hutchinson, Shear coefficients for Timoshenko beam theory, Journal of Applied Mechanics 68 (2001) 87–92.

[20] G.S. Duncan, M. Tummond, T. Schmitz, An investigation of the dynamic absorber effect in high-speed machining, International Journal of Machine Tools and Manufacture 45 (2005) 497–507.